Materials Advances

ROYAL SOCIETY OF CHEMISTRY

PAPER

View Article Online
View Journal | View Issue

Cite this: *Mater. Adv.*, 2022, 3, 5900

A study on the effect of phase conversion of tungsten nanostructures on their electrochemical energy storage performance†

Visakh V. Mohan,[a] P. M. Anjana[a] and R. B. Rakhi *[bc]

Received 28th April 2022,
Accepted 2nd June 2022

DOI: 10.1039/d2ma00475e

rsc.li/materials-advances

Herein, we report the synthesis of tungsten based nanostructures such as WO_3, WO_{3-x} ($W0_{2.72}$:WS_2), and WS_2 through a facile single step hydrothermal technique. The optical, structural, and morphological studies are conducted, and the electrochemical performance of each electrode material is evaluated in a symmetric two electrode configuration. An enhancement in the electrochemical energy storage performance has been observed on changing the phase from WO_3 to WS_2, which may be due to the accompanying changes in morphology and surface area. At 1 A g^{-1}, the symmetric supercapacitors with WO_3, WO_{3-x}, and WS_2 electrodes exhibit specific capacitance values of 62, 86, and 215 F g^{-1}, respectively. At a power density of 0.76 kW kg^{-1}, the WO_3, WO_{3-x} and WS_2 based devices offer energy density values of 5.5, 7.6, and 19.1 W h kg^{-1}, respectively. The WS_2 electrode based supercapacitor retains an excellent cycling stability rate of 97% over 10 000 continuous charge discharge cycles.

1. Introduction

Supercapacitors and batteries are the two crucial realms of energy storage technology that have gained immense attention. Batteries are characterized by their high specific energy value, whereas supercapacitors are known for their high specific power.[1–4] Combining the properties of supercapacitors and batteries led to the invention of 'supercapattery'.[1–4] Before establishing supercapattery on a large scale, the fabrication of novel electrode materials for supercapacitors need to be encouraged. Theoretical models suggest that tungsten-based nanostructures can enhance electrochemical performance because of their superior optical and electronic properties. Herein, we focus on investigating the activity of the tungsten-based nanostructures as supercapacitor electrode materials.

As a predominant non-ferrous metal, the well-organized implementation and high-quality processing of tungsten resources are of great importance. Synthesis of tungsten-based nanostructures in large quantities offers immense opportunities to produce desired nanodevices. The high theoretical capacitance of tungsten oxide (WO_3), along with its convenient crystalline features, tunable bandgap, earth abundance, economic viability, and eco-friendly nature, makes this material a promising candidate for a supercapacitor electrode material.[5–10] The electrochemical method, sol-gel synthesis, microwave treatments, *etc.*, are the most reported synthesis techniques of WO_3 nanomaterials.[11–14] Specific capacitance (C_{sp}) values of 58.3 and 42.6 F g^{-1}, respectively, have been reported for electrodeposited rGO-WO_3 and WO_3 electrodes at a current density of 1 A g^{-1}.[15] In 2021, Feiyan Shi *et al.* reported a solid-state type supercapacitor based on 3D porous lignin-derived carbon/WO_3 with a specific capacitance of 432 F g^{-1} at 0.5 A g^{-1} and cycling stability of 86.6% after 10 000 cycles.[16] In another study, a solid-state device was fabricated using WO_3 (monoclinic phase) and 2D Ti_3C_2Tx on a 3D graphene foam with a C_{sp} value of 145.2 F g^{-1} at 5 mV s^{-1}.[17] All these studies were conducted in a three-electrode asymmetric configuration. Not many reports are available on the electrochemical performance of WO_3 in the symmetric two-electrode configuration.

The tungsten oxide materials can be found in various colours, like green, violet, and dark blue, owing to some oxygen-deficient non-stoichiometric materials, namely $WO_{2.83}$, $WO_{2.8}$ and $WO_{2.72}$, *etc.*[18–24] Growth time, growth temperature, synthesis methods, and the precursors used for the synthesis determine the colour change. The morphological structure and the optoelectronic properties of these compounds vary. Still, the materials are stable in various conditions, like dry or humid atmospheres and in the dark or under light irradiation. The properties such as carrier concentration, charge transport,

[a] *Department of Physics University of Kerala, Kariavattom, Thiruvananthapuram, Kerala 695581, India*
[b] *Material Sciences and Technology Division, CSIR-National Institute of Interdisciplinary Science and Technology (CSIR-NIIST), Thiruvananthapuram, Kerala 695019, India. E-mail: rakhiraghavanbaby@niist.res.in; Tel: +91 9497113659*
[c] *Academy of Scientific and Innovative Research (AcSIR), Ghaziabad 201002, India*

† Electronic supplementary information (ESI) available. See DOI: https://doi.org/10.1039/d2ma00475e

electrical conductivity, *etc.*, are improved within the semiconductor by the shallow donor energy level created by the oxygen vacancies. Yingying Li *et al.* reported an oxygen vacancy study on tungsten oxide materials. In his work, the change of colour of WO_3 material from yellow to dark blue ($WO_{2.72}$) due to the effect of hydrogen treatment (as a photothermocatalyst) was explained.[22] The oxygen vacancies of the WO_3 material and its photocatalytic applications were also reported by Michael Sachs *et al.*[23] It is of great value to explore the charge storage mechanism of tungsten oxides possessing different contents of oxygen vacancies for supercapacitor applications since this field has not been investigated much.

Tungsten disulfide (WS_2) is another trending material among transition-metal dichalcogenides (TMD), which is considered a next generation 2D TMD for energy storage applications.[24–28] WS_2 possesses many optoelectronic properties similar to tungsten oxides. According to the theoretical models, in comparison with other TMDs, WS_2 exhibits the highest mobility because of its reduced effective mass. The material has high theoretical capacitance and a large surface area.[24–28] So WS_2 can be considered a promising material for supercapacitor applications. Recently Amrita De *et al.* reported a WS_2/PANI composite supercapacitor for high-frequency AC filtering applications. The symmetric supercapacitor based on WS_2/PANI shows a capacitance of 72.27 F g^{-1} at 1 A g^{-1} and energy density and power density value of 6.42 W h kg^{-1} and 399.9 W kg^{-1}, respectively. The device shows 98% capacitance retention after 10 000 cycles.[29] In another symmetric configuration study, WS_2/RGO composite electrodes were fabricated by S. Ratha *et al.* The device shows a specific capacitance of 350 F g^{-1} at a scan rate of 2 mV s^{-1}. But the bare WS_2 shows a C_{sp} of 70 F g^{-1} only.[30] In the asymmetric three-electrode configuration, K.V. Raghavendra *et al.* fabricated a $WS_2/ZnCo_2O_4$ composite electrode material for supercapacitor applications in 2021. The device shows a specific capacity of 154.74 mAh g^{-1}. The device exhibited 80.08% rate capability and 96.34% stability up to 4000 cycles. Here also, the bare WS_2 electrode exhibited a specific capacity of 48.61 mAh g^{-1} only.[31] Reports suggest that the WS_2 material shows poor performance as an electrode material for supercapacitors, whereas WS_2 performs exceptionally well in combination with other organic/inorganic composite materials. Considering the innate potential of WS_2, the outcome has not reached up to the expectation. So it is necessary to focus more research on this area.

The present work is devoted to the experimental investigation of the supercapacitor performance of tungsten oxide nanostructures and tungsten sulfide synthesized through a single-step and facile hydrothermal synthesis method. WO_3, WO_{3-x}, and WS_2 nanostructures are synthesized and optimized. The electrochemical energy storage performance of the materials in symmetric two-electrode configurations is evaluated, and the results are discussed.

2. Experimental

2.1 Materials

Thiourea: CH_4N_2S (Sigma-Aldrich; ≥99.0%), sodium chloride: NaCl (Sigma-Aldrich; ≥99%), sodium tungstate dihydrate: $Na_2WO_4.2H_2O$ (Sigma-Aldrich; ≥99%), hydrochloric acid: HCl (Sigma-Aldrich; 37%).

2.2 Synthesis

2.2.1 Method 1: synthesis of WO_3. To synthesize a WO_3 nanomaterial through a hydrothermal process, $Na_2WO_4.2H_2O$ (sodium tungstate dihydrate) was used as the tungsten source. As a direct growth agent, sodium chloride was used.

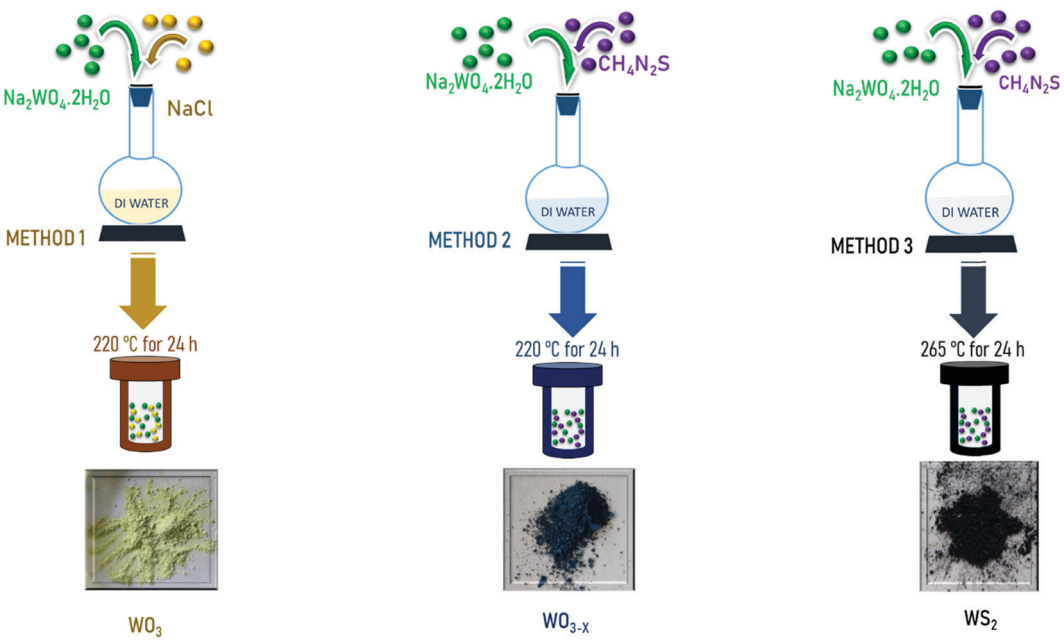

Fig. 1 Schematic of the synthesis of tungsten based nanostructures.

Both $Na_2WO_4.2H_2O$ and NaCl were dissolved in 60 ml of deionized water at 50 °C with 40 min vigorous magnetic stirring. After complete dissolution, the pH level of the solution was adjusted by using HCl and it was placed in a Teflon-lined stainless steel autoclave (100 ml). The temperature maintained for the entire process is 220 °C for 24 h. Finally, the product obtained was taken and washed and dried at 80 °C for 20 h. The colour of the product is yellow, as shown in Fig. 1.

2.2.2 Method 2: synthesis of WO_{3-x}. The entire synthesis process was repeated, as mentioned in Section 2.2.1, except that CH_4N_2S was used instead of NaCl, all the other processes being the same. Finally, a dark blue colour precipitate was obtained, as shown in Fig. 1.

2.2.3 Method 3: synthesis of WS_2. The entire synthesis process was repeated, as mentioned in Section 2.2.2, except that the temperature for the hydrothermal synthesis was increased to 265 °C from 220 °C, for the same period of time that is 24 h. At the end of the hydrothermal synthesis process, a black colour precipitate was obtained, as shown in Fig. 1.

2.3 General characterization

The structural and optical investigations of the samples were done using XRD (Bruker D_8 Advance) and Raman spectroscopy (Horiba Jobin Yvon micro spectrometer). Also the model Jasco 6800 was used for FTIR spectroscopy (400 to 2500 cm^{-1}). Morphological analyses were conducted by using a Carl ZEISS FESEM. A Tristar 3000 was used for Brunauer–Emmett–Teller (BET) surface area analysis. An Octane Elect was used for EDS Elemental composition analysis. An FEI, Tecnai G230LaB6 was employed for TEM analysis. XPS analysis was done using a PHI 5000 Versa Probe II (ULVAC-PHI Inc.).

2.4 Symmetric device fabrication and performance studies

For electrochemical performance studies and device fabrication, first WO_3, WO_{3-x}, and WS_2 samples were ultrasonicated for 10–15 min using ethanol. After that, each one was deposited separately over a carbon cloth having an area of 1 cm^2. These deposited electrodes were then dried at nearly 70 °C for the time period of 6 h.

The electrochemical studies were performed in a two-electrode configuration by using an electrochemical workstation (VMP3 biologic). The two active electrodes were set apart with an insulating separator (Celgard 3400). The electrolyte used for the fabrication of the device is KOH. The assembly was then put together in a test cell, EL-Cell, for electrochemical measurements.

The specific capacitance value for the symmetric device is calculated by the equation,

$$C_{sp} = \frac{2i}{m\left(\frac{\Delta V}{\Delta t}\right)} \quad (1)$$

Here 'i' stands for the cathodic current, $\frac{\Delta V}{\Delta t}$ represents the slope of the discharge curve, and 'm' stands for the mass of active electrode material in each electrode.

3. Results and discussion

3.1 Material characterization

The XRD spectra of the WO_3, WO_{3-x}, and WS_2 materials are shown in Fig. 2. All peaks of the WO_3 sample are indexed. The observed peaks closely match the JCPD file number 00-072-1465, corresponding to the monoclinic crystal system (Space Group $P21/n$) of WO_3 with the predominant peak showing orientation toward the 002 crystalline plane. The XRD pattern of the WO_{3-x} sample shows a peak broadening compared to the XRD spectra of WO_3. The peak broadening suggests a change in crystallite size, which is due to the introduction of sulfur. The presence of a non-stoichiometric compound was also identified from these observations. The non-stoichiometric compound of tungsten oxide is $WO_{2.72}$, which is confirmed from the JCPD file number 00-073-2177. All peaks of the WO_{3-x} sample are indexed and the crystalline planes indicate that the prepared sample was a monoclinic phase of $WO_{2.72}$ with space group $P2/m$. Similar observations were also seen in Raman analysis. The XRD pattern of the WS_2 sample matches the hexagonal phase of WS_2 with Space Group $P63/mmc$ (JCPDS file number: 00-008-0237).

A peak broadening has been observed on moving toward the WS_2 sample from WO_3 due to the change in crystallite size. The crystallite size has been calculated from the Debye–Scherrer equation given in the ESI† as eqn (1).

The Raman spectra of WO_3, WO_{3-x}, and WS_2 are shown in Fig. 3a. In the case of the WO_3 sample, the sharp peaks observed at 808 cm^{-1} and 716 cm^{-1} are allocated to the stretching mode of the tungsten atom with the nearest oxygen atoms. The other two peaks observed at 324 cm^{-1} and 270 cm^{-1}

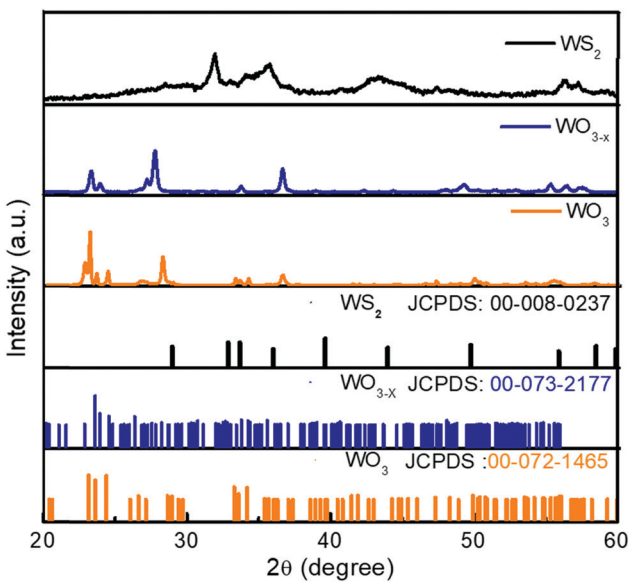

Fig. 2 XRD Pattern of WO_3, WO_{3-x} and WS_2 samples.

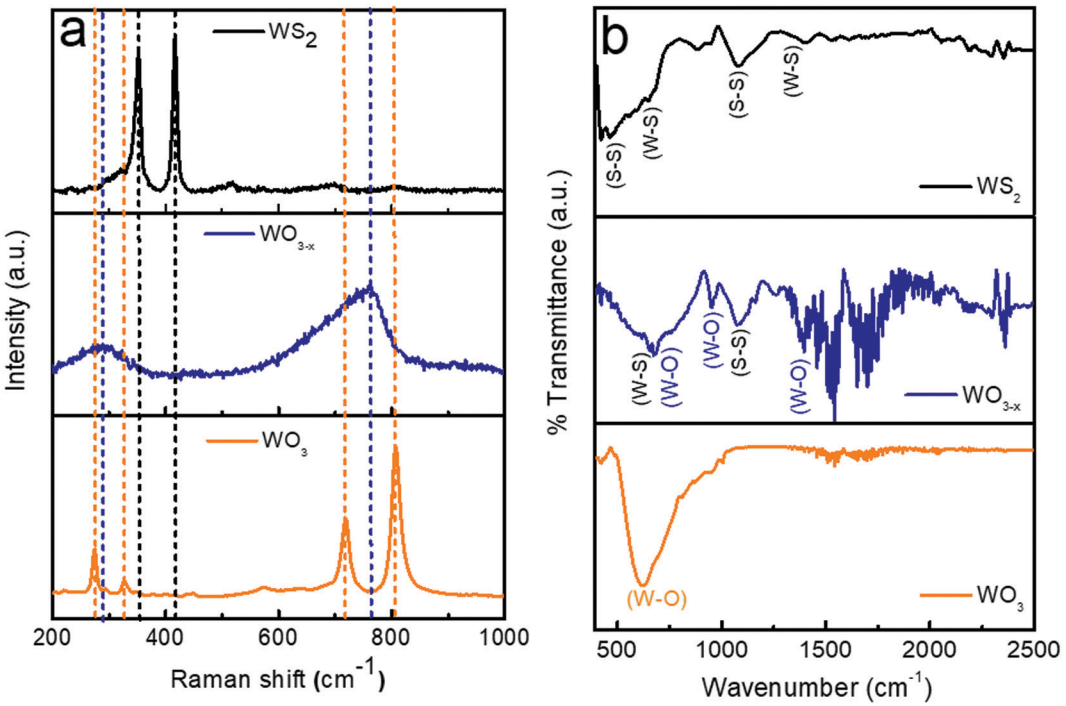

Fig. 3 (a) Raman spectra, and (b) FTIR spectra of the WO_3, WO_{3-x} and WS_2 samples.

correspond to the W–O–W bending mode of vibration.[14,22,42] No impurity phases were observed. When coming to the WO_{3-x} sample, with sulfur treatment, a broadening has been observed in the characteristics of the Raman bands. The broadening suggests that there is a weakening in crystallization. Also a shift to a lower wavenumber has been observed which might be due to the introduction of oxygen vacancies. The presence of non-stoichiometric compounds like $WO_{2.72}$ was identified from these observations. The shift in the W–O stretching mode of vibration to the lower wavenumber region might be due to the oxygen vacancy,which would have lead to the rise in the interplanar distance and lengths of W–O bonds. Similar observations were also reported by Y. Li *et al.*[22] Finally, while analyzing the WS_2 sample, it has been noted that all the peaks corresponding to the W-O bands have vanished. The presence of oxygen and non-stoichiometric tungsten oxide compounds entirely disappeared. No other impurity phases were detected. This is achieved by the controlled synthesis strategy adopted during the hydrothermal synthesis process, as mentioned in Section 2.2.3. Two dominant peaks were observed at 347 ± 2 cm^{-1} and 415 ± 2 cm^{-1} corresponding to the in-plane and out-of-plane vibration of the WS_2.[30,32]

The FTIR is closely associated with molecular vibration and instructions related to the bonding and structure of molecules. The FTIR spectra of WO_3, WO_{3-x}, and WS_2 samples (wavenumber between 400 and 2500 cm^{-1}) are shown in Fig. 3b. The dominant peak at 616 cm^{-1} detected for the WO_3 sample corresponds to the stretching and bending vibrations for O–W–O and W–O–W in WO_3.[33,34] No other dominant peaks were detected, which guaranteed the purity of the tungsten oxide sample. In the WO_{3-x} sample, the peak observed at 670 ± 2 cm^{-1} corresponds to the W–O–W stretching mode of vibration, and the peak detected at nearly 956 cm^{-1} is attributed to the W–O stretching vibration of the sample, and the peak at 1396 cm^{-1} is attributed to the O–H bending vibration in W–OH.[33,34] S–S/W–S bonds were also detected due to the presence of WS_2 in the sample. The peak detected at 650 cm^{-1} indicates W–S stretching and bending vibrations in WS_2 and that at nearly 1082 cm^{-1} refers to the S–S vibrations in the as-prepared sample.[32,35,46,47] Hence in the WO_{3-x} sample, a composite formation of $WO_{2.72}$:WS_2 was confirmed. The shift in peaks were observed due to the formation of WS_2 in the WO_{3-x} sample. These results match with the XRD results. In the case of the WS_2 sample, three dominant peaks were observed. The first two peaks detected at 650 cm^{-1} and 1399 cm^{-1} are attributed to W–S stretching and bending vibrations (similar to the WO_{3-x} sample), and the third one detected at nearly 1082 cm^{-1} shows the existence of S–S bonds. Also the peak observed at 452 cm^{-1} suggests the confirmation of the existence of the S–S stretching vibrations of WS_2.[32,35,46,47]

The optical properties of WO_3, WO_{3-x}, and WS_2 were analyzed by the UV–visible spectroscopy technique. The optical band gap of each sample was calculated by the diffuse reflection spectra (DRS) method with the help the Kubelka–Munk equation[36] and shown in Fig. S1a–c in the ESI.† The optical bandgap of WO_3 is 2.5 eV, that of WO_{3-x} is 2.2 eV and for the WS_2 sample is 1.7 eV. A decrease in bandgap was observed when coming from WO_3/WO_{3-x} to WS_2. The reduction in bandgap for the WO_{3-x} and WS_2 samples might be due to oxygen vacancies. The oxygen vacancies in the samples produce in-gap donor states, thereby trying to decrease the gap between the Conduction Band Minima (CBM) and Valance Band Maxima (VBM).[36] The oxygen vacancy and bandgap narrowing studies were also

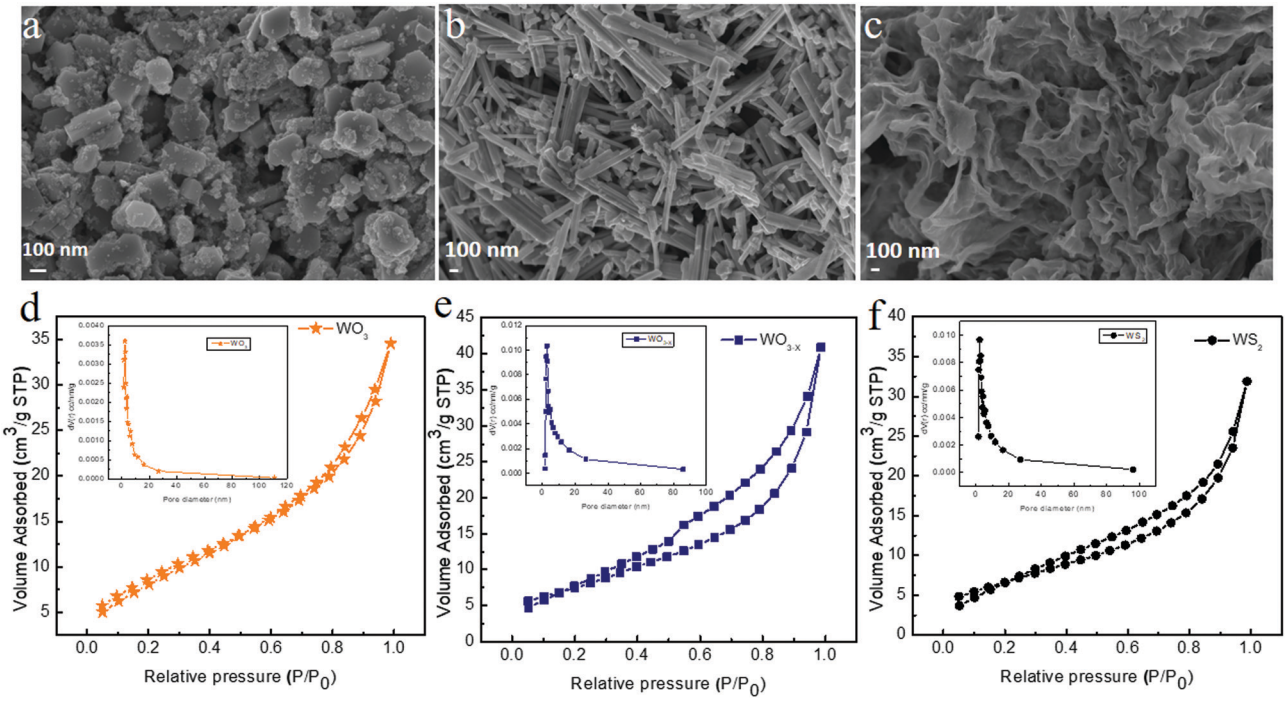

Fig. 4 FESEM images of (a) WO_3, (b) WO_{3-x} and (c) WS_2, and nitrogen adsorption and desorption isotherms of (d) WO_3, (e) WO_{3-x} and (f) WS_2.

reported in the case of the ZnO material by Junpeng Wang *et al.*[37]

XPS analysis was carried out to investigate the oxygen vacancy study of the WO_{3-x} sample, and the results are shown in the ESI† in Fig. S1d to f. The analysis reveals that three oxidation states of *W* are found in the WO_{3-x} sample as +6, +5 and +4, confirming the presence of $WO_{2.72}$ and WS_2 in the sample.

The morphology and the microstructure of the samples were examined by FESEM and TEM measurements, respectively. Fig. 4 shows the FESEM images of WO_3, WO_{3-x}, and WS_2 samples synthesized *via* the hydrothermal technique. The WO_3 sample exhibited a nanoplate-like structure, whereas the WO_{3-x} sample exhibited nanorod/nanowire-like morphologies,[48] as evident from Fig. 4a and b. In the WO_{3-x} sample, layered flakes were moderately wrapped around the nanowires. The change in morphology might be due to the effect of the sulfur precursor in the sample.[38–40,48] The average diameter of the WO_3 nanoplate was around 260 nm. The average diameter of the nanorod was around 84 nm. And the average length of the nanorod was 950 nm. The WS_2 sample exhibited a nanosheet/nanoflake-like morphology, as shown in Fig. 4c. The high temperature assisted synthesis of the WS_2 sample helps in the conversion of WO_3 nonorod/nanowire to WS_2 nanosheet/nanoflake-like morphology.[32] The substitution of oxygen by sulfur (conversion of the oxide to sulfur) takes place due to the effect of temperature. A similar observation was reported for the SnS based material in 2020.[44]

The growth mechanism of the different morphologies of WO_3/WO_{3-x} can be explained according to the following equations[45]

$$Na_2WO_4{\cdot}2H_2O \Rightarrow 2Na^+ + WO_4^{2-} + 2H_2O \quad (2)$$

$$2Na^+ + WO_4^{2-} + 2HCl \Rightarrow H_2WO_4 + 2NaCl \quad (3)$$

$$H_2WO_4 \Rightarrow WO_3\ (\text{crystal nucleus}) + H_2O \quad (4)$$

$$WO_3\ (\text{crystal nucleus})/WO_3\ (\text{different morphologies})$$

The incomplete sulfidation of the tungsten oxide resulted in the morphological deviation of plate-like TMO to nanorods of the composite $WO_{2.72}$:WS_2. The complete sulfidation of tungsten oxide favours the formation of sulfide layers over the TMO. The continuous sulfidation leads to the change in morphology from nanorods to nanosheets.

The nanosheet-like morphology can contribute to maximum electrolyte accessible surface area. The existence of an immense quantity of redox-active regions will contribute to better conductivity for WS_2, thereby improving the electrochemical performance of the electrode material.[32]

The BET surface analysis provides details regarding the pore volume and surface area of the material. Fig. 4d–f show the nitrogen adsorption and desorption isotherms of WO_3, WO_{3-x}, and WS_2 electrode materials. The BET results confirm that the WO_3 electrode material has a surface area of 7.3 $m^2\ g^{-1}$ with an average pore radius of 3.2164 nm. The WO_{3-x} electrode material possesses a surface area of 23.789 $m^2\ g^{-1}$ with an average pore radius of 4.5996 nm. The WS_2 electrode material shows a comparatively higher surface area of 24.486 $m^2\ g^{-1}$ with an average pore radius of 4.0390 nm. These results are in good agreement with our FESEM analysis. The isotherms of all these samples come under the type IV profile. The hysteresis loop also confirms that all three electrode materials were mesoporous in nature.[32,41]

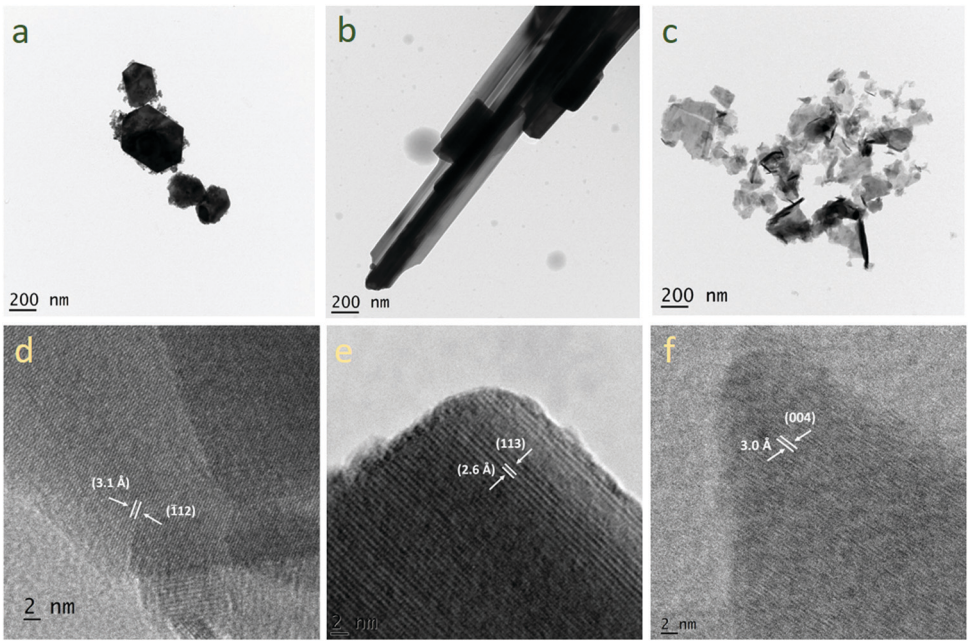

Fig. 5 TEM images of (a) WO_3, (b) WO_{3-x} and (c) WS_2 and HR-TEM images of (d) WO_3, (e) WO_{3-x} and (f) WS_2 samples.

Fig. 5a–c, respectively, show the bright field TEM images of WO_3, WO_{3-x} and WS_2. Nanoplate-like morphology was confirmed for the WO_3 material. The nanoplate-like morphology then changes to nanorod/nanowire-like morphology in the case of the WO_{3-x} sample. Nanosheet-like morphology was confirmed for the WS_2 electrode material. Fig. 5d shows the HR-TEM image of the WO_3 electrode material for which the d spacing is 3.1 Å, indicating that the reflection is from the (−112) plane. Fig. 5e shows the HR-TEM image of WO_{3-x} electrode materials, where the d spacing is 2.6 Å and the reflection is from the (113) plane. Fig. 5f shows the HR-TEM image of the WS_2 electrode material for which the d spacing is 3 Å, indicating the reflection from the (004) plane.

3.2. Fabrication of WO_3, WO_{3-x} and WS_2 based symmetric supercapacitors and electrochemical performance studies

The cyclic voltammograms (CV) of the three symmetric supercapacitors based on WO_3, WO_{3-x}, and WS_2 electrode materials were investigated between the potential range 0 to 0.8 V at different scan rates from 5 to 200 mV s^{-1}, and the results are shown as Fig. S2 in the ESI.† Fig. 6a depicts the comparison CV curves of WO_3, WO_{3-x}, and WS_2 based supercapacitors at a scan rate of 20 mV S^{-1}. The quasi rectangle structure of the CV curve of all three electrode materials suggests that the charge storage mechanism is a combination of the double layer and the pseudocapacitive behaviors. The percentage of surface capacitive and diffusion contributions for each electrode material has to be confirmed later. The comparison of the galvanostatic charge–discharge (GCD) measurements of the devices was conducted between the potential ranges of 0 to 0.8 V at different current densities from 1 to 5 A g^{-1}. The GCD curves for the supercapacitors at a constant current density of 1 A g^{-1} are shown in Fig. 6b. The deviation from the ideal triangular shape of the GCD curves indicates the contribution from the pseudocapacitive and EDLC charge storage mechanism. The specific capacitance values of devices were calculated from the GCD measurements by using eqn (1). At 1 A g^{-1}, symmetric supercapacitors based on WO_3, WO_{3-x}, and WS_2 electrode materials exhibited C_{sp} values of 62, 86, and 215 F g^{-1}, respectively. The superior capacitive performance of the WS_2 based supercapacitor can be attributed to the large electrolyte accessible surface area offered by the WS_2 material.

The electrochemical charge storage mechanism of WO_3/$W0_{3-x}$ in KOH electrolyte can be expressed using eqn (5) as:[45]

$$WO_3 + xK^+ + xe^- \Rightarrow KxWO_3. \quad (5)$$

The storage mechanism of WS_2 can be explained by using equations 6 and 7,[32]

$$WS_2 + K^+ + e^- \Leftrightarrow WS\text{--}SK \text{ (faradaic)} \quad (6)$$

$$(WS_2)_{surface} + K^+ + e^- \Leftrightarrow (WS_2\text{--}K^+)_{surface} \text{ (non faradaic)} \quad (7)$$

The variations in the specific capacitance values at different current densities are shown in Fig. 6c. A decline in specific capacitance value with increasing current density is observed. This behavior matches the general trend in the rate performance of energy storage devices. The ions from the electrolyte could get more access to the pores that exist in the inner structure of the electrode material at a lower scan rate. This process increases the specific capacitance at lower scan rates.

For the practical application of the device, the stability or charge retention rate should be higher. Here, the fabricated symmetric devices of WO_3, WO_{3-x}, and WS_2 possess excellent charge retention rates. The WS_2 based device demonstrated 97% capacitance retention even after 10 000 cycles at 5 A g^{-1}

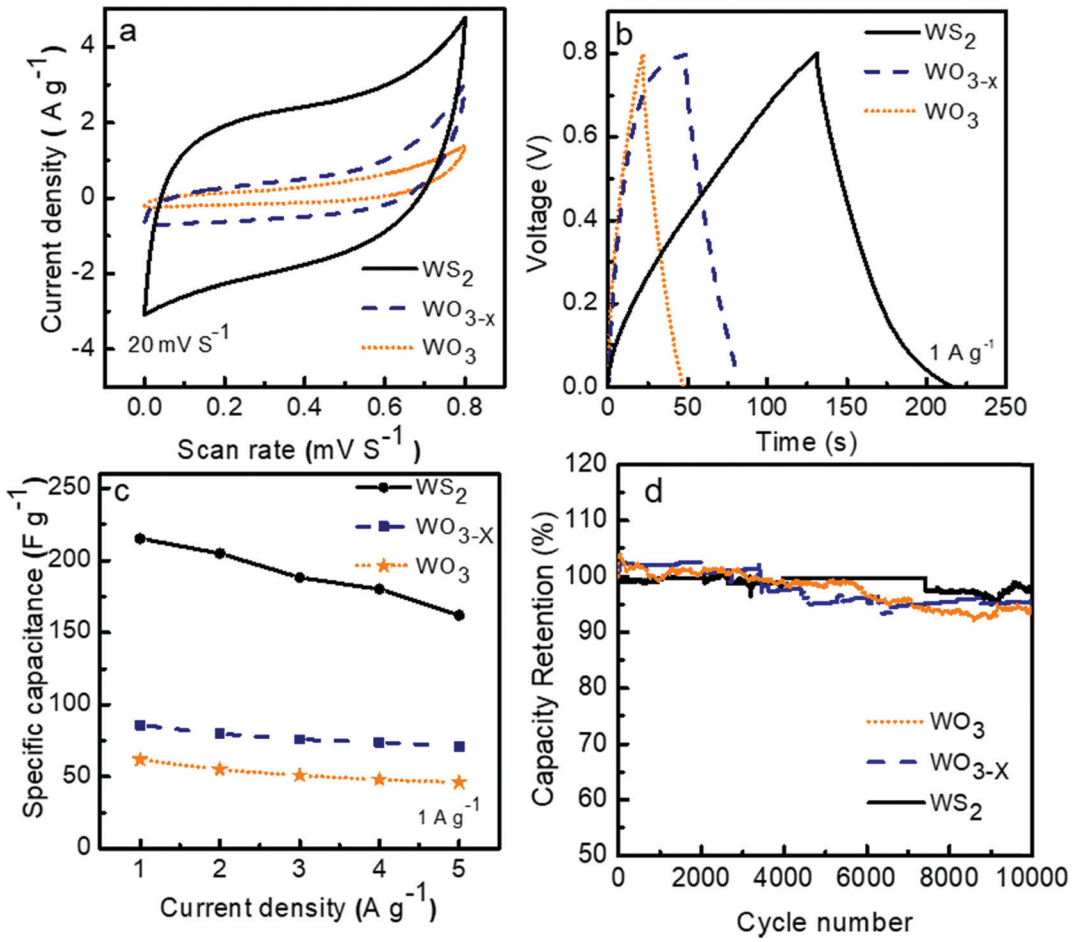

Fig. 6 (a) CV curve of WO_3, WO_{3-x} and WS_2 at 20 mV s^{-1}, (b) GCD curve of WO_3, WO_{3-x} and WS_2 at 1 A g^{-1}, (c) variation of the specific capacitance with current density, (d) the capacitance retention of the WO_3, WO_{3-x} and WS_2 electrode material over 10 000 cycles.

current density, which is much better than the other two devices, as shown in Fig. 6d. The WO_3 and WO_{3-x} electrode material based devices exhibited nearly 93% and 96% capacitance retention even after 10 000 cycles. The cyclic stability of the WS_2 based device at a high current density of 20 A g^{-1} over 6500 cycles has also been done, shown in Fig. S3 in the ESI.†

The morphology and microstructure of the materials were further evaluated using SEM and TEM measurements after the

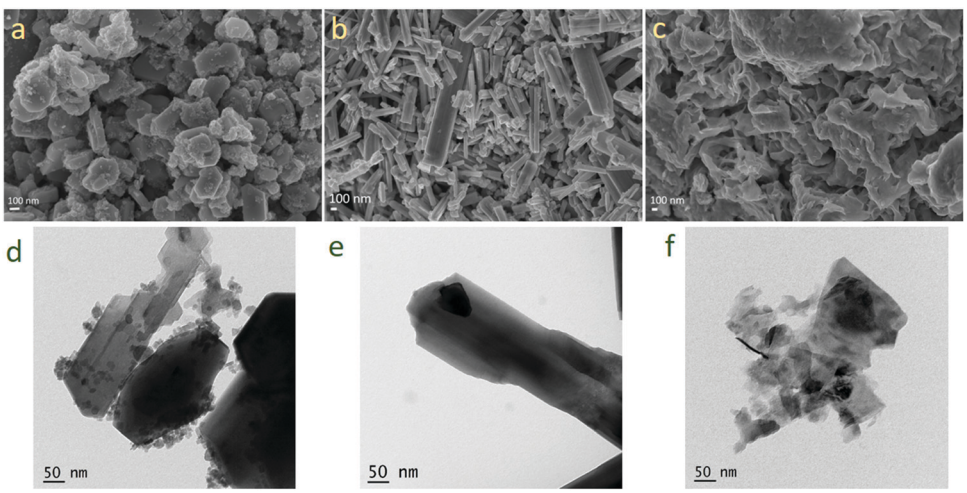

Fig. 7 SEM images of (a) WO_3, (b) WO_{3-x} and (c) WS_2 and TEM images of (d) WO_3, (e) WO_{3-x}, and (f) WS_2 after the cycling stability test.

Table 1 Comparison of the symmetrical device performance of WO_3 and WS_2 based electrode materials with the literature

Electrode Material	Electrolyte	Current density/scan rate	Capacitance (F g^{-1})	Stability (%)	Energy density (W h kg^{-1})	Ref.
rGO-WO_3	1 M H_2SO_4	1 A g^{-1}	58.3	—	—	15
WO_3 Monoclinic	1 M H_2SO_4	1 A g^{-1}	42.6	—	—	15
WO_3 Monoclinic	6 M KOH	10 mV S^{-1}	37	—	—	42
WO_3/CNT	2 M KOH	1 A g^{-1}	50	81	—	43
Co (5%) doped WO_3/*f*-CNT	2 M KOH	1 A g^{-1}	60.14	83	—	43
WO_3 Monoclinic	6 M KOH	1 A g^{-1}	62	93	5.5 @0.76 kW kg^{-1}	This work
WO_{3-x}	6 M KOH	1 A g^{-1}	86	96	7.6 @ 0.79 kW kg^{-1}	This work
WS_2/PANI	1 M Na_2SO_4	1 A g^{-1}	72.27	98	6.42 @ 0.4 kW kg^{-1}	29
WS_2	1 M Na_2SO_4	2 mV S^{-1}	70	—	—	30
WS_2 Nanoflower	6 M KOH	1 A g^{-1}	119	100	10.57 @ 0.8 kW kg^{-1}	32
WS_2 Nanosheet	6 M KOH	1 A g^{-1}	215	97	19.1 @0.8 kW kg^{-1}	This work

stability studies. Fig. 7 shows the FESEM images and TEM images of the samples after cycling stability measurements. The samples did not show any noticeable changes in the morphology and microstructure.

Table 1 shows the comparison of the symmetrical device performance of WO_3 and WS_2 electrode materials with the literature.

Fig. 8a–c show the Nyquist plots of WO_3, WO_{3-x}, and WS_2 supercapacitors. The EIS measurements of the three symmetric devices were conducted over 0.01 Hz to 100 kHz frequency. The diameter of the semicircle region represents the charge transfer resistance (R_{ct}) of the electrode material. Symmetric supercapacitors based on WO_3, WO_{3-x}, and WS_2 materials exhibit R_{ct} values of 8.9, 7.6, and 5.8 Ω, respectively. With the lowest R_{ct} value, the WS_2 electrode offers better conductivity and excellent specific capacitance. The fitting of the EIS plots using ZSimpWIN3.21 software is illustrated in Fig. S4a–c of the ESI.† The Bode plots of the supercapacitors are shown in Fig. S4d (ESI†). Energy and power density values have been calculated using eqn (8) and (9):

$$S_E = \frac{C_{sp} \times v^2}{2 \times 3.6} \text{ W h kg}^{-1} \quad (8)$$

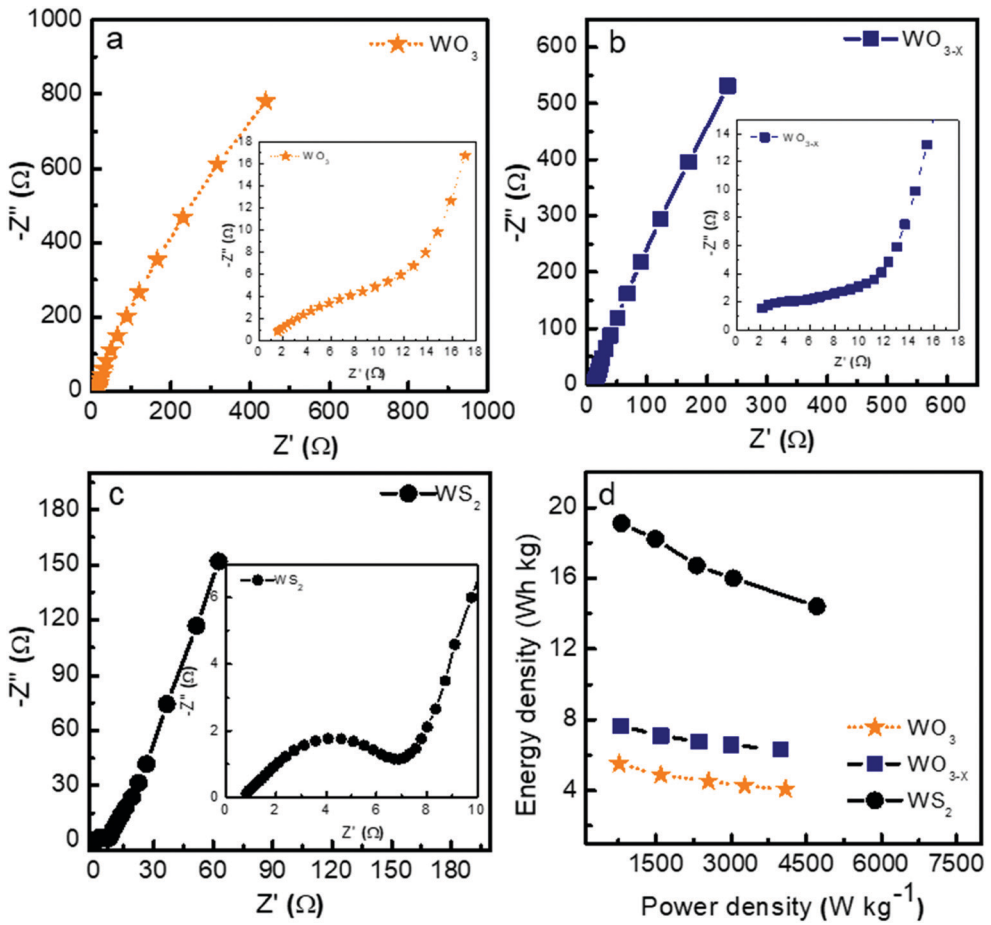

Fig. 8 Nyquist plot of (a) WO_3, (b) WO_{3-x} and (c) WS_2, and (d) Ragone plot.

$$S_P = \frac{S_E \times 3600}{\Delta t} \text{ W kg}^{-1} \quad (9)$$

where C_{sp} is the specific capacitance, V is the cell voltage, Δt is the discharge time in seconds, S_E is the specific energy in W h Kg^{-1} and S_P is the specific power in W kg^{-1}. The Ragone plot is shown in Fig. 8d. At a power density of 0.76 kW kg^{-1}, the WO_3, WO_{3-x}, and WS_2 based devices offer energy density values of 5.5, 7.6, and 19.1 W h kg^{-1}, respectively.

The contribution of charge storage can be calculated from Trasatti's method and Dunn's method, as shown in Fig. S5 of the ESI.† The present study demonstrates that the WS_2 based supercapacitor shows excellent electrochemical performance compared to the other two devices due to its higher surface area and better charge transfer resistance. An increment has also been seen in specific capacitance, energy density, and stability rate while coming from WO_3 to WS_2 nanostructures due to the changes in morphology and surface area.

The WO_3, WO_{3-x}, and WS_2 nanomaterials show excellent electrochemical performance, making them ideal for supercapacitor electrode materials. The asymmetric combinations of these electrode materials can also be explored.[49–52]

4. Conclusion

WO_3, WO_{3-x}, and WS_2 nanomaterials were successfully synthesized through a single-step hydrothermal technique. The electrochemical energy storage performance of the as-prepared nanomaterials was evaluated in symmetric two-electrode configurations. At a constant current density of 1 A g^{-1}, the symmetric supercapacitors with WO_3, WO_{3-x}, and WS_2 electrodes exhibited specific capacitance values of 62, 86, and 215 F g^{-1}, respectively. At a power density of 0.76 kW kg^{-1}, the WO_3, WO_{3-x}, and WS_2 based devices demonstrated energy density values of 5.5, 7.6, and 19.1 W h kg^{-1}, respectively. The WS_2 based device exhibited superior electrochemical performance with excellent cycling stability of 97%, even after 10 000 consecutive GCD cycles at 5 A g^{-1}.

Conflicts of interest

There are no conflicts to declare.

Acknowledgements

The authors are very grateful to CUSAT for the support in FESEM measurements, Stick CUSAT for HRTEM analysis, and CLIF, University of Kerala for XRD characterization. R.B. Rakhi acknowledges financial support from IC MAP project (DST/TMD/IC-MAP/2K20/01) from Technology Mission Division (Energy, Water & all Others), Department of Science & Technology, Ministry of Science & Technology, Government of India.

References

1 Y. Li, B. Huang, X. Zhao, Z. Luo, S. Liang, H. Qin and L. Chen, Zeolitic imidazolate framework-L-assisted synthesis of inorganic and organic anion-intercalated hetero-trimetallic layered double hydroxide sheets as advanced electrode materials for aqueous asymmetric super-capacitor battery, *J. Power Sources*, 2022, **527**, 231149, DOI: **10.1016/j.jpowsour.2022.231149**.

2 B. Huang, H. Wang, S. Liang, H. Qin, Y. Li, Z. Luo, C. Zhao, L. Xie and L. Chen, Two-dimensional porous cobalt–nickel tungstate thin sheets for high performance supercapattery, *Energy Storage Mater.*, 2020, **32**, 105–114, DOI: **10.1016/j.ensm.2020.07.014**.

3 S. Liang, H. Wang, Y. Li, H. Qin, Z. Luo and L. Chen, Ternary synergistic transition metal oxalate 2D porous thin sheets assembled by 3D nanoflake array with high performance for supercapattery, *Appl. Surf. Sci.*, 2021, **567**, 150809, DOI: **10.1016/j.apsusc.2021.150809**.

4 B. Huang, W. Wang, T. Pu, J. Li, C. Zhao, L. Xie and L. Chen, Rational design and facile synthesis of two-dimensional hierarchical porous MVO (M = Co, Ni and Co−Ni) thin sheets assembled by ultrathin nanosheets as positive electrode materials for high-performance hybrid supercapacitors, *Chem. Eng. J.*, 2019, **375**, 121969, DOI: **10.1016/j.cej.2019.121969**.

5 F. Zheng, H. Gong, Z. Li, W. Yang, J. Xu, P. Hu, Y. Li, Y. Gong and Q. Zhen, Tertiary structure of cactus-like WO3 spheres self-assembled on Cu foil for supercapacitive electrode materials, *J. Alloys Compd.*, 2017, **712**, 345–354, DOI: **10.1016/j.jallcom.2017.04.094**.

6 S. Yao, F. Qu, G. Wang and X. Wu, Facile hydrothermal synthesis of WO3 nanorods for photocatalysts and supercapacitors, *J. Alloys Compd.*, 2017, **724**, 695–702, DOI: **10.1016/j.jallcom.2017.07.123**.

7 V. Lokhande, A. Lokhande, G. Namkoong, J. H. Kim and T. Ji, Charge storage in WO 3 polymorphs and their application as supercapacitor electrode material, *Results Phys.*, 2019, **12**, 2012–2020, DOI: **10.1016/j.rinp.2019.02.012**.

8 K. W. Kim, T. Y. Yun, S. H. You, X. Tang, J. Lee, Y. Seo, Y. T. Kim, S. H. Kim, H. C. Moon and J. K. Kim, Extremely fast electrochromic supercapacitors based on mesoporous WO3 prepared by an evaporation-induced self-assembly, *NPG Asia Mater.*, 2020, **12**, 84, DOI: **10.1038/s41427-020-00257-w**.

9 M. Faraji, R. Khalilzadeh Soltanahmadi, H. Mohammadzadeh Aydisheh and B. Mostafavi Bavani, 2.0-V flexible all-solid-state symmetric supercapacitor device with high electrochemical performance composed of MWCNTs-WO3-graphite sheet, *Ionics*, 2020, **26**, 3003–3013, DOI: **10.1007/s11581-020-03502-y**.

10 T. Wang, H. Liu, J. Li and H. A. Munir, Facile Preparation of h-WO3/Carbon Cloth Nanocomposite and Its Electrochemical Properties for Supercapacitors, *ChemistrySelect*, 2020, **5**, 7704–7713, DOI: **10.1002/slct.202001733**.

11 D. Susanti, A. A. G. P. Diputra, L. Tananta, H. Purwaningsih, G. E. Kusuma, C. Wang, S. Shih and Y. Huang, WO3 nanomaterials synthesized via a sol-gel method and calcination for use as a CO gas sensor, *Front. Chem. Sci. Eng.*, 2014, **8**, 179–187, DOI: **10.1007/s11705-014-1431-0**.

12 X. Song, Y. Zheng and H. Yin, Synthesis and Electrochemical Performance of One-Dimensional WO3 and WO3·

0.33H2O Nanostructures, *Curr. Nanosci.*, 2012, **8**, 120–124, DOI: **10.2174/157341312799362304**.

13 G. F. Samu, K. Pencz, C. Janáky and K. Rajeshwar, On the electrochemical synthesis and charge storage properties of WO3/polyaniline hybrid nanostructures, *J. Solid State Electrochem.*, 2015, **19**, 2741–2751, DOI: **10.1007/s10008-015-2820-0**.

14 D. Nunes, A. R. Fragoso, T. Freire, M. Matias, A. C. Marques, R. F. de, P. Martins, E. Fortunato and A. Pimentel, Ultrafast Microwave Synthesis of WO3 Nanostructured Films for Solar Photocatalysis, *Phys. Status Solidi RRL*, 2021, **15**, 1–10, DOI: **10.1002/pssr.202100196**.

15 Y. E. Firat, Pseudocapacitive energy storage properties of rGO-WO3 electrode synthesized by electrodeposition, *Mater. Sci. Semicond. Process.*, 2021, **133**, 105938, DOI: **10.1016/j.mssp.2021.105938**.

16 F. Shi, J. Li, J. Xiao, X. Zhao, H. Li, Q. An, S. Zhai, K. Wang, L. Wei and Y. Tong, Three-dimensional hierarchical porous lignin-derived carbon/WO3 for high-performance solid-state planar micro-supercapacitor, *Int. J. Biol. Macromol.*, 2021, **190**, 11–18, DOI: **10.1016/j.ijbiomac.2021.08.183**.

17 A. M. Patil, J. Wang, S. Li, X. Hao, X. Du, Z. Wang, X. Hao, A. Abudula and G. Guan, Bilateral growth of monoclinic WO3 and 2D Ti3C2Tx on 3D free-standing hollow graphene foam for all-solid-state supercapacitor, *Chem. Eng. J.*, 2021, **421**, 127883, DOI: **10.1016/j.cej.2020.127883**.

18 Z. Shen, Z. Zhao, J. Wen, J. Qian, Z. Peng and X. Fu, Role of Oxygen Vacancies in the Electrical Properties of WO_{3-x} Nano/Microrods with Identical Morphology, *J. Nanomater.*, 2018, **2018**, 7802589, DOI: **10.1155/2018/7802589**.

19 F. Zhan, Y. Liu, K. Wang, X. Yang, M. Liu, X. Qiu, J. Li and W. Li, Oxygen-Deficient Nanofiber WO_{3-x}/WO_3 Homojunction Photoanodes Synthesized via a Novel Metal Self-Reducing Method, *ACS Appl. Mater. Interfaces*, 2019, **11**, 39951–39960, DOI: **10.1021/acsami.9b13326**.

20 W. Wang, A. Janotti and C. G. Van De Walle, Role of oxygen vacancies in crystalline WO3, *J. Mater. Chem. C*, 2016, **4**, 6641–6648, DOI: **10.1039/c6tc01643j**.

21 R. Sato, N. Kawamura and H. Tokumaru, The coloration of tungsten-oxide film by oxygen deficiency and its mechanism, *Appl. Surf. Sci.*, 2008, **254**, 7676–7678, DOI: **10.1016/j.apsusc.2008.01.161**.

22 Y. Li, C. Wang, H. Zheng, F. Wan, F. Yu, X. Zhang and Y. Liu, Surface oxygen vacancies on WO 3 contributed to enhanced photothermo-synergistic effect, *Appl. Surf. Sci.*, 2017, **391**, 654–661, DOI: **10.1016/j.apsusc.2016.07.042**.

23 M. Sachs, J. S. Park, E. Pastor, A. Kafizas, A. A. Wilson, L. Francàs, S. Gul, M. Ling, C. Blackman, J. Yano, A. Walsh and J. R. Durrant, Effect of oxygen deficiency on the excited state kinetics of WO3 and implications for photocatalysis, *Chem. Sci.*, 2019, **10**, 5667–5677, DOI: **10.1039/c9sc00693a**.

24 M. I. A. Abdel Maksoud, R. A. Fahim, A. E. Shalan, M. Abd Elkodous, S. O. Olojede, A. I. Osman, C. Farrell, A. H. Al-Muhtaseb, A. S. Awed, A. H. Ashour and D. W. Rooney, *Advanced materials and technologies for supercapacitors used in energy conversion and storage: a review*, Springer International Publishing, 2021. , DOI: **10.1007/s10311-020-01075-w**.

25 C. Lee, B. G. Jeong, S. J. Yun, Y. H. Lee, S. M. Lee and M. S. Jeong, Unveiling Defect-Related Raman Mode of Monolayer WS_2 *via* Tip-Enhanced Resonance Raman Scattering, *ACS Nano*, 2018, **12**, 9982–9990, DOI: **10.1021/acsnano.8b04265**.

26 C. Lan, C. Li, J. C. Ho and Y. Liu, 2D WS_2: From Vapor Phase Synthesis to Device Applications, *Adv. Electron. Mater.*, 2021, **7**, 1–36, DOI: **10.1002/aelm.202000688**.

27 D. Ovchinnikov, A. Allain, Y.-S. Huang, D. Dumcenco and A. Kis, Electrical Transport Properties of Single-Layer WS_2, *ACS Nano*, 2014, **8**, 8174–8181, DOI: **10.1021/nn502362b**.

28 F. Wang, S. Li, M. A. Bissett, I. A. Kinloch, Z. Li and R. J. Young, Strain engineering in monolayer WS_2 and WS_2 nanocomposites OPEN ACCESS, (2020).

29 A. De Adhikari, N. Shauloff, Y. Turkulets, I. Shalish and R. Jelinek, Tungsten-Disulfide/Polyaniline High Frequency Supercapacitors, *Adv. Electron. Mater.*, 2021, **7**, 1–8, DOI: **10.1002/aelm.202100025**.

30 S. Ratha and C. S. Rout, Supercapacitor electrodes based on layered tungsten disulfide-reduced graphene oxide hybrids synthesized by a facile hydrothermal method, *ACS Appl. Mater. Interfaces*, 2013, **5**, 11427–11433, DOI: **10.1021/am403663f**.

31 K. Venkata Guru Raghavendra, T. V. M. Sreekanth, J. Kim and K. Yoo, Novel hydrothermal synthesis of jasmine petal-like nanoflower $WS_2/ZnCo_2O_4$ as efficient electrode material for high-performance supercapacitors, *Mater. Lett.*, 2021, **285**, 129133, DOI: **10.1016/j.matlet.2020.129133**.

32 V. V. Mohan, M. Manuraj, P. M. Anjana and R. B. Rakhi, WS_2 Nanoflowers as Efficient Electrode Materials for Supercapacitors, *Energy Technol.*, 2022, **10**, 1–7, DOI: **10.1002/ente.202100976**.

33 K. Shahzad, M. B. Tahir, M. Ashraf, T. Nawaz, N. R. Khalid and M. R. Kabli, Interfacial Growth of Activated Carbon on WO3 Nanoplates for Enhanced Photocatalytic Activity by Surface Plasmon Resonance, *Plasmonics*, 2020, **15**, 1205–1212, DOI: **10.1007/s11468-020-01135-5**.

34 H. Najafi-Ashtiani, A. Bahari, S. Gholipour and S. Hoseinzadeh, Structural, optical and electrical properties of WO3–Ag nanocomposites for the electro-optical devices, *Appl. Phys. A: Mater. Sci. Process.*, 2018, **124**, 24, DOI: **10.1007/s00339-017-1412-5**.

35 H. S. Vaziri, A. Shokuhfar and S. S. S. Afghahi, Synthesis of WS_2/CNT hybrid nanoparticles for fabrication of hybrid aluminum matrix nanocomposite, *Mater. Res. Express*, 2020, **7**, 025034, DOI: **10.1088/2053-1591/ab70e1**.

36 P. J. Boruah, R. R. Khanikar and H. Bailung, Synthesis and Characterization of Oxygen Vacancy Induced Narrow Band-gap Tungsten Oxide (WO3−x) Nanoparticles by Plasma Discharge in Liquid and Its Photocatalytic Activity, *Plasma Chem. Plasma Process.*, 2020, **40**, 1019–1036, DOI: **10.1007/s11090-020-10073-3**.

37 J. Wang, Z. Wang, B. Huang, Y. Ma, Y. Liu, X. Qin, X. Zhang and Y. Dai, Oxygen vacancy induced band-gap narrowing and enhanced visible light photocatalytic activity of ZnO, *ACS Appl. Mater. Interfaces*, 2012, **4**, 4024–4030, DOI: **10.1021/am300835p**.

38 G. A. Asres, A. Dombovari, T. Sipola, R. Puskás, A. Kukovecz, Z. Kónya, A. Popov, J. F. Lin, G. S. Lorite, M. Mohl, G. Toth, A. Lloyd Spetz and K. Kordas, A novel WS_2 nanowire-nanoflake hybrid material synthesized from WO3 nanowires in sulfur vapor, *Sci. Rep.*, 2016, **6**, 1–7, DOI: **10.1038/srep25610**.

39 S. Zeb, G. Sun, Y. Nie, Y. Cui and X. Jiang, Synthesis of highly oriented WO3 nanowire bundles decorated with Au for gas sensing application, *Sens. Actuators, B*, 2020, **321**, 128439, DOI: **10.1016/j.snb.2020.128439**.

40 G. Tang, H. Tang, C. Li, W. Li and X. Ji, Surfactant-assisted hydrothermal synthesis and characterization of WS_2 nanorods, *Mater. Lett.*, 2011, **65**(23–24), 3457–3460, DOI: **10.1016/j.matlet.2011.07.033**.

41 Z. A. Alothman, A review: Fundamental aspects of silicate mesoporous materials, *Materials*, 2012, **5**, 2874–2902, DOI: **10.3390/ma5122874**.

42 V. V. Mohan, P. M. Anjana and R. B. Rakhi, Materials Today: Proceedings One pot synthesis of tungsten oxide nanomaterial and application in the field of flexible symmetric supercapacitor energy storage device, *Mater. Today Proc.*, 2022, DOI: **10.1016/j.matpr.2022.04.046**.

43 R. Dhilip Kumar, Y. Andou and S. Karuppuchamy, Facile synthesis of Co–WO3/functionalized carbon nanotube nanocomposites for supercapacitor applications, *J. Mater. Sci.: Mater. Electron.*, 2017, **28**, 5425–5434, DOI: **10.1007/s10854-016-6203-9**.

44 V. V. Mohan, K. C. Akshaya, A. S. Asha, M. K. Jayaraj and K. P. Vijayakumar, Effect of substrate temperature on the optoelectronic properties of chemically sprayed SnS thin films, *Mater. Today Proc.*, 2019, **39**, 1978–1980, DOI: **10.1016/j.matpr.2020.08.512**.

45 K. Sun, F. Hua, S. Cui, Y. Zhu, H. Peng and G. Ma, An asymmetric supercapacitor based on controllable WO3nanorod bundle and alfalfa-derived porous carbon, *RSC Adv.*, 2021, **11**, 37631–37642, DOI: **10.1039/d1ra04788d**.

46 M. Latha and J. Vatsala Rani, WS_2/Graphene Composite as Cathode for Rechargeable Aluminum-Dual Ion Battery, *J. Electrochem. Soc.*, 2020, **167**, 070501, DOI: **10.1149/2.0012007jes**.

47 M. V. Santhosh, R. Geethu and K. S. Devaky, A novel, facile, and efficient two-step hydrothermal route for WS_2 nanosheets and its optimistic exposure as competent industrial-level sonocatalyst, *J. Mater. Sci.: Mater. Electron.*, 2021, **32**, 9357–9367, DOI: **10.1007/s10854-021-05599-x**.

48 M. Weil and W. D. Schubert, The beautiful colours of tungsten oxides, *ITIA Newsl.*, 2013, 1–12.

49 L. Wang, X. Tan, Q. Zhu, Z. Dong, X. Wu, K. Huang and J. Xu, The universality applications of MoS2@MnS heterojunction hollow microspheres for univalence organic or multivalence aqueous electrolyte energy storage device, *J. Power Sources*, 2022, **518**, 230747, DOI: **10.1016/j.jpowsour.2021.230747**.

50 J. Xu, Z. Dong, K. Huang, L. Wang, Z. Wei, L. Yu and X. Wu, Flexible design of large layer spacing V-MoS2@C cathode for high-energy zinc-ion battery storage, *Scr. Mater.*, 2022, **209**, 114368, DOI: **10.1016/j.scriptamat.2021.114368**.

51 J. Xu, Q. Liu and Z. Dong, Interconnected MoS_2 on 2D Graphdiyne for Reversible Sodium Storage, *ACS Appl. Mater. Interfaces*, 2021, **13**, 46, DOI: **10.1021/acsami.1c15484**.

52 J. Xu, S. Zhang, Z. Wei, W. Yan, X. Wei and K. Huang, Orientated VSe2 nanoparticles anchored on N-doped hollow carbon sphere for high-stable aqueous energy application, *J. Colloid Interface Sci.*, 2021, **585**, 12–19, DOI: **10.1016/j.jcis.2020.11.065**.